Journal of Environmental Chemical Engineering 14 (2026) 121561

Contents lists available at ScienceDirect

Journal of Environmental Chemical Engineering

journal homepage: www.elsevier.com/locate/jece

Engineering the 1T/2H-$MoSe_2$ phase junction as an S-scheme cocatalyst for boosted photocatalytic hydrogen evolution

Linlin Gao, Yamei Huang, Jiayi Meng, Yifan Liao, Zizheng Wang, Quanmei Zhou, Yuchen Wei, Wei-Lin Dai *

State Key Laboratory of Porous Materials for Separation and Conversion, Shanghai Key Laboratory of Molecular Catalysis and Innovative Materials, Department of Chemistry, Fudan University, Shanghai 200438, PR China

ARTICLE INFO

Keywords:
1 T/2H-$MoSe_2$ nanoflowers
CdZnS nanorods
S-scheme heterojunction
Charge transfer channel
Photocatalytic hydrogen evolution

ABSTRACT

This study underscores the critical role of phase engineering in boosting the photocatalytic hydrogen evolution performance of $MoSe_2$-based heterostructures. The metallic (1 T) and semiconducting (2 H) phases of $MoSe_2$ were rationally synthesized and integrated with CdZnS nanorods to construct a 1 T/2H-$MoSe_2$/CdZnS hybrid photocatalyst. The optimized composite exhibits an exceptional H_2 evolution rate of 44.9 $mmol \cdot g^{-1} \cdot h^{-1}$, representing a 5.4-fold enhancement over pristine CdZnS and significantly outperforming the 2H-$MoSe_2$/CdZnS control. Comprehensive spectroscopic, electrochemical, and density functional theory (DFT) analyses reveal that this superior activity arises from the synergistic effects of the 1 T phase, including enhanced electrical conductivity, a narrowed bandgap, and an abundance of catalytically active sites. These features collectively promote visible-light absorption and facilitate the efficient separation of photogenerated electron–hole pairs. Ultraviolet photoelectron spectroscopy (UPS) and DFT calculations further corroborate the formation of an S-scheme charge transfer pathway at the heterojunction interface, which enables spatial separation of redox potentials and accelerates interfacial electron transfer. Notably, the 1 T/2H-$MoSe_2$ surface exhibits an optimized hydrogen adsorption free energy, approaching the thermoneutral ideal for proton reduction. This work not only provides fundamental insights into phase-dependent interfacial charge dynamics but also establishes a rational design strategy for precious-metal-free photocatalysts capable of efficiently converting solar energy into chemical fuels.

1. Introduction

The growing worldwide demand for energy, coupled with serious environmental issues associated with fossil fuel consumption, has intensified the focus on developing clean and renewable alternative energy sources [1]. Solar energy, owing to its abundance and sustainability, stands out as a highly viable solution. Of the many strategies for utilizing solar power, the use of photocatalysis to split water for hydrogen generation represents a highly effective pathway to transform sunlight directly into chemical energy that is both dense and capable of being stored, thereby addressing both energy and environmental challenges [2–4]. The core of this technology lies in developing efficient, stable, and low-cost photocatalysts [5–7].

Among numerous photocatalytic materials, metal sulfides, particularly CdS and its zinc solid solution ($Cd_{1-\delta}Zn_{\delta}S$, CdZnS), have shown great potential for H_2 evolution when exposed to light. The reason lies in their suitable energy band structure, generally between 2.4 and 2.6 electronvolts, combined with efficient uptake of light within the visible wavelength range [8–11]. Introducing Zn^{2+} ions into the crystalline framework to create CdZnS solid solutions not only modulates the electronic structure and extends light absorption but also effectively suppresses photocorrosion and enhances photostability [12]. However, like many single semiconductors, CdZnS suffers from inherent limitations such as inefficient separation of photogenerated charges and fast recombination of e^- and holes [13–15].

To address these issues, coupling with cocatalysts to construct composite interfaces has emerged as a powerful strategy to enhance the dissociation of photogenerated charges and reduce the reaction overpotential [4,16]. Recently, two-dimensional transition metal dichalcogenides (TMDs), such as MoS_2, have attracted significant research interest and have been extensively explored as alternatives to noble metal cocatalysts, owing to their high density of catalytically active edge

* Corresponding author.
E-mail address: wldai@fudan.edu.cn (W.-L. Dai).

https://doi.org/10.1016/j.jece.2026.121561
Received 19 November 2025; Received in revised form 24 January 2026; Accepted 30 January 2026
Available online 31 January 2026

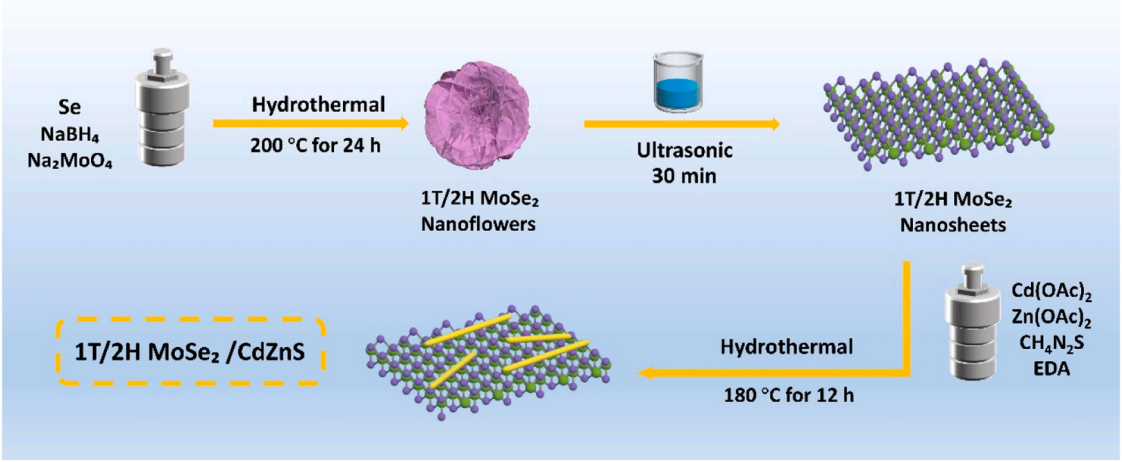

Scheme 1. Schematic illustration for the synthesis of 1 T/2H-$MoSe_2$/CdZnS.

locations and platinum-like hydrogen adsorption free energy [17–19]. Among various TMDs, molybdenum diselenide ($MoSe_2$) exhibits a narrower bandgap, higher intrinsic conductivity, and a theoretically more favorable hydrogen adsorption Gibbs free energy (ΔG_H^*), rendering it a more promising candidate than MoS_2 [20–23]. It is noteworthy that $MoSe_2$ exists in two distinct crystalline phases: the metastable metallic phase (1T-$MoSe_2$) and semiconducting phase (2H-$MoSe_2$), which is thermodynamically stable [24]. Both theoretical and electrocatalytic studies have revealed that the 1 T phase possesses significantly enhanced electron transport properties and a higher density of catalytically accessible sites distributed over its flat surface, in contrast to alternative phases, leading to remarkably enhanced hydrogen evolution reaction (HER) kinetics [25,26]. This makes structural modulation a viable approach for optimizing its cocatalytic performance.

Currently, several studies have attempted to incorporate $MoSe_2$ (mostly in the 2 H phase or mixed phases) with various semiconductors (*e.g.*, CdS, g-C_3N_4) and observed moderate improvements in hydrogen production performance [25]. Concurrently, the successful synthesis of the 1T-$MoSe_2$ phase has been reported, demonstrating exceptional activity in electrocatalytic HER [24]. However, most studies have not thoroughly investigated the differential impact of $MoSe_2$'s distinct structural configurations on its cocatalytic functionality. In particular, a systematic comparison of the enhancement effects of different $MoSe_2$ structures (*e.g.*, metallic 1 T *vs.* semiconducting 2 H) on the same host photocatalyst (*e.g.*, CdZnS), coupled with an in-depth exploration of the underlying mechanism, remains insufficient. Such a comparative study is crucial for understanding the structure-performance relationship of cocatalysts.

Therefore, this research seeks to investigate the influence of the $MoSe_2$ phase in photocatalytic hydrogen evolution. Nanosheets of hybrid-phase $MoSe_2$ and single-phase $MoSe_2$ were synthesized through controlled preparation and subsequently composited with CdZnS nanorods to construct 1 T/2H-$MoSe_2$/CdZnS and 2H-$MoSe_2$/CdZnS composite photocatalysts. Performance tests revealed that metallic 1T-$MoSe_2$ as a cocatalyst significantly outperformed its semiconducting 2 H counterpart. Specifically, the H_2 evolution rate achieved by the 1 T/2H-$MoSe_2$/CdZnS was 1.2 times greater than 2H-$MoSe_2$/CdZnS composite and 5.4 times higher than the pristine CdZnS material. Through a combination of photoelectrochemical characterizations and theoretical calculations, the underlying mechanisms responsible for the performance disparity were systematically examined, clarifying the unique advantages of the 1 T phase in enhancing charge separation efficiency and accelerating interfacial electron transfer. This work not only confirms that structural modulation is an effective strategy for designing high-performance cocatalysts but also provides fundamental insights as well as practical validation to guide the informed choice and strategic development of highly active cocatalysts in solar-driven hydrogen production systems.

2. Experimental

2.1. Synthesis of 1 T/2H-$MoSe_2$ nanoflowers

A mixture of $NaBH_4$ (4 mmol), Se powder (2 mmol), and $Na_2MoO_4{\cdot}2\ H_2O$ (1 mmol) was thoroughly ground and gradually added to 35 mL of deionized water under vigorous mechanical stirring for a duration of 30 min. The resulting solution was sealed in a Teflon-lined stainless-steel high-pressure reactor and maintained at 200 °C for 24 h. Following the completion of the reaction and natural cooling to ambient conditions, the dark-colored precipitate was isolated by centrifugation, repeatedly rinsed with deionized water and absolute ethanol to remove impurities, and finally dried under vacuum at 60 °C.

2.2. Synthesis of 2 H $MoSe_2$ nanoflowers

0.5 mmol sodium molybdate dihydrate was dissolved in deionized water (10 mL) to form a clear solution. Separately, Se powder (1.2 mmol) was dispersed in 35 % hydrazine hydrate solution (10 mL). These two solutions were then merged under continuous magnetic stirring for 30 min to ensure homogeneity. The combined reaction mixture was transferred into an autoclave and maintained at 200 °C for 24 h. After the reaction concluded and the system cooled naturally to room temperature, the resulting black precipitate was isolated by centrifugation, purified through repeated washing with deionized water and ethanol, and finally dried under vacuum at 60 °C.

2.3. Synthesis of CdZnS nanorods

Cadmium acetate (0.5 mmol) and zinc acetate (0.5 mmol) were successively introduced into a mixed solvent consisting of 24 mL ethylenediamine and 12 mL deionized water (2:1 vol ratio), followed by the addition of thiourea (3 mmol). The mixture was stirred vigorously for 30 min to achieve complete dissolution and homogenization. The resulting solution was sealed in a hydrothermal reactor with a polytetrafluoroethylene liner and heated at 180 °C for 12 h. Upon cooling to ambient temperature, the yellow solid product was collected by centrifugation, rinsed thoroughly to eliminate residual ions and organics, and dried under reduced pressure at 60 °C

2.4. Synthesis of $MoSe_2$/CdZnS composites

A predetermined amount of $MoSe_2$ powder was added to the

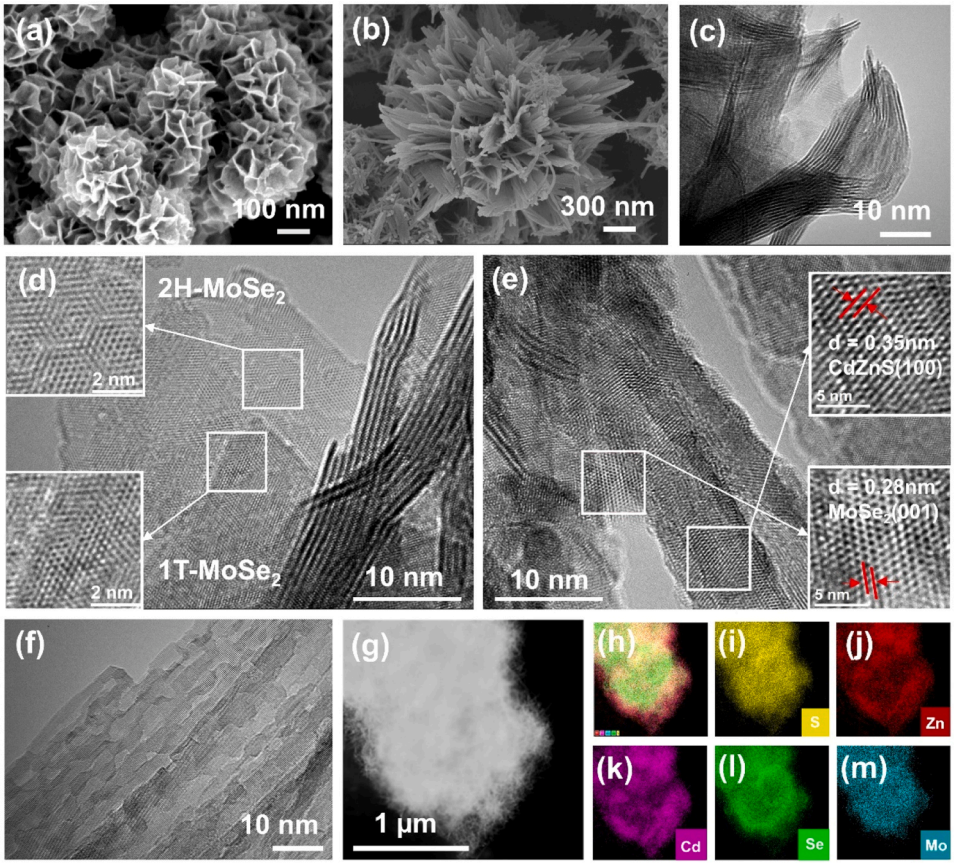

Fig. 1. SEM images of (a) 1 T/2H-MS, (b) 1 T/2H-MS/CZS, TEM images of (c, d) 1 T/2H-MS, (e) 1 T/2H-MS/CZS, (f) CdZnS, (g-m) SEM and EDS of 1 T/2H-MS/CZS.

precursor solution containing Cd and Zn salts, and dispersed uniformly via ultrasonic treatment combined with magnetic stirring for 30 min. A precisely measured quantity of pre-synthesized $MoSe_2$ powder was then introduced into the precursor solution prepared in Section 2.3 for CdZnS synthesis and uniformly dispersed through 30 min of sonication-assisted agitation. Subsequently, the solution underwent hydrothermal processing at 180 °C for 12 h. Upon completion and cooling, the greenish solid product was recovered by centrifugation, washed multiple times with water and ethanol, and dried in a vacuum oven at 60 °C. To facilitate discussion, the composite containing mixed 1 T/2H-$MoSe_2$ is denoted as 1 T/2H-MS/CZS, while the one based on predominantly 2H-$MoSe_2$ is labeled as 2H-MS/CZS.

2.5. Characterization and activity test

Detailed information on materials, characterization, DFT calculation, and catalytic performance test can be found in Supporting Information.

3. Results and discussion

3.1. Morphology and structure characterization

Scheme 1 provides a schematic overview of the composite catalyst preparation. The process began with the fabrication of $MoSe_2$ nanoflowers using a hydrothermal approach. Subsequently, CdZnS nanorods were grown in situ on the 1 T/2H-MS nanosheets via a secondary hydrothermal treatment, resulting in the formation of intimately coupled 1 T/2H-MS/CZS composites.

The structural morphology and fine microstructure of the synthesized samples were investigated using field emission transmission electron microscopy (FE-TEM) and scanning electron microscopy (SEM). Fig. S1 shows the clustered structure of CdZnS assembled from nanorod-like aggregates. The $MoSe_2$ component displays a three-dimensional architecture resembling a flower, while the layered configuration of the 1 T/2H-$MoSe_2$ heteronanostructure can be clearly observed in Fig. 1 (a & c). Uniform dispersion of CdZnS nanorods across the surface of the 1 T/2H-MS nanosheets is observed in the SEM micrographs (Fig. 1(b)). Elemental mapping obtained from energy-dispersive X-ray spectroscopy (Fig. 1(h–m)) illustrates a spatially uniform dispersion of Cd, Zn, S, Mo, and Se, thereby supporting the effective integration of all components within the hybrid material. A close-up TEM image in Fig. 1(d) highlights the differing structural features of the 1 T and 2 H phases of $MoSe_2$. In the 1 T phase, interlayer stacking appears less compact, with visible distortions in the lattice manifested as irregular fringe intervals and localized imperfections [27]. Conversely, the 2 H phase maintains a regular interlayer spacing and exhibits a well-defined crystalline order [28]. HR-TEM analysis (Fig. 1(e)) shows lattice patterns with interplanar distances of 0.35 nm and 0.28 nm, which are assigned to the (100) crystal facet of CdZnS and the (001) facet of $MoSe_2$, respectively.

The crystalline phase and structural purity of the prepared materials were analyzed by X-ray diffraction. As shown in Fig. 2(a), characteristic reflections observed at 55.4°, 26.9°, 37.3°, 44.3°, 25.2°, 48.6°, 51.8°, and 28.6° are assigned to the (004), (002), (102), (110), (100), (103), (200), and (101) lattice planes of CdZnS, respectively. All observed diffraction peaks can be indexed to three distinct crystalline phases: cadmium sulfide (CdS, JCPDS card No. 77–2306) with hexagonal wurtzite structure (space group $P6_3mc$), zinc sulfide (ZnS, JCPDS card No. 36–1450) with cubic zincblende structure (space group F -3 m), and molybdenum diselenide ($MoSe_2$, JCPDS card No. 87–2419) with hexagonal 2 H polytype (space group $P6_3/mmc$). The absence of extraneous diffraction peaks indicates high phase purity, while the sharpness of the reflections confirms excellent crystallinity of the synthesized materials.

With increasing $MoSe_2$ content, the characteristic XRD peaks of

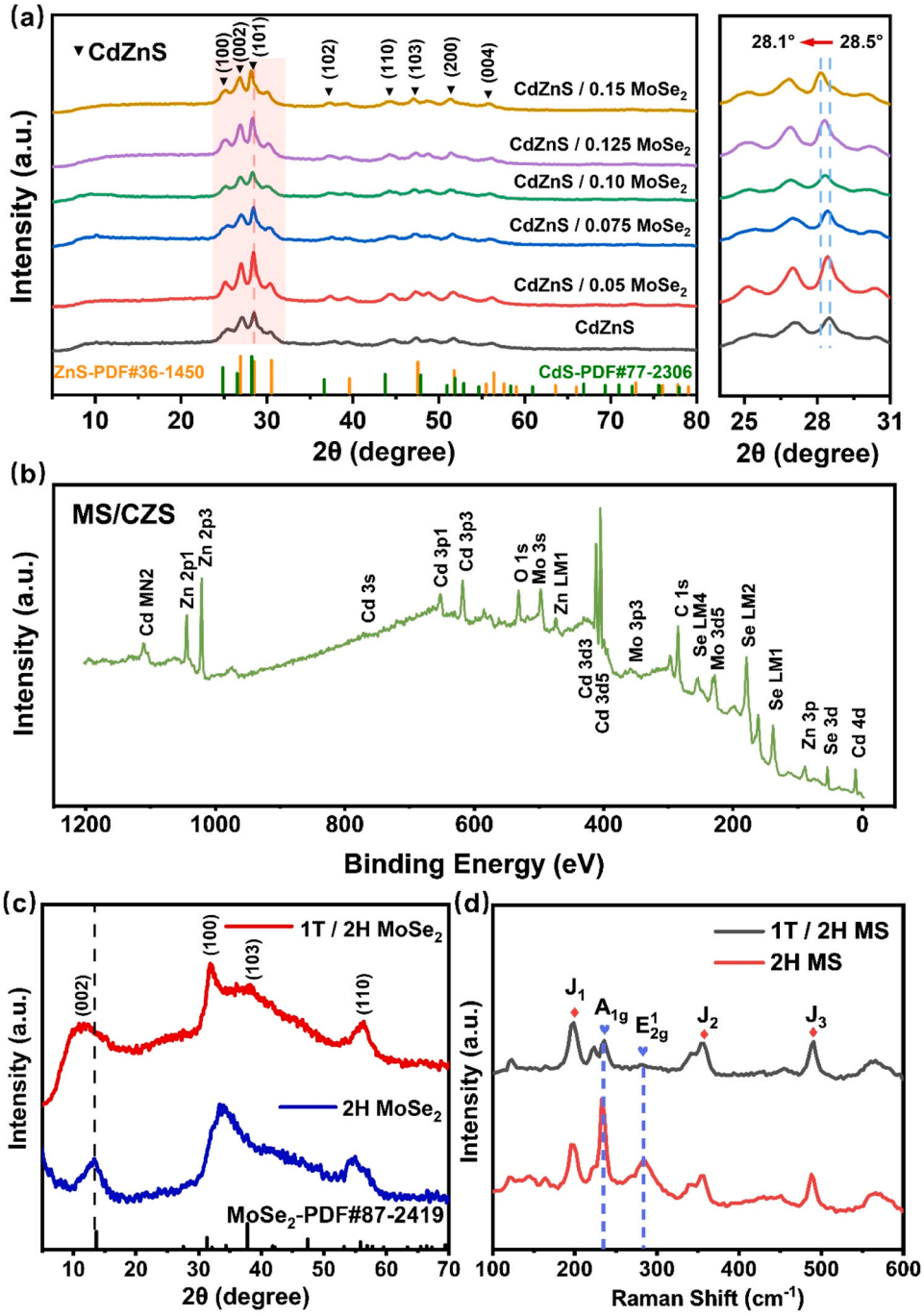

Fig. 2. (a) XRD patterns of *x*-MS/CZS, (b) Survey XPS spectra of MS/CZS, (c) XRD patterns of 1 T/2H-MS, 2 H MS, (d) Raman spectra of 1 T/2H-MS, 2 H MS.

CdZnS systematically shifted toward lower diffraction angles. The composite containing 15 % $MoSe_2$ exhibited a measurable shift of approximately 0.4° toward lower 2θ values compared to pure CdZnS, indicating significant lattice expansion in the CdZnS phase. According to Bragg's law ($n\lambda = 2d\cdot\sin\theta$), this angular decrease directly corresponds to increased interplanar spacing (d), primarily resulting from the partial substitution of S^{2-} ions (ionic radius = 1.84 Å) by larger Se^{2-} ions (ionic radius = 1.98 Å) diffusing from the $MoSe_2$ phase into the CdZnS lattice. The progressive nature of this shift with increasing $MoSe_2$ concentration supports the anion exchange mechanism. Additionally, interfacial strain due to lattice mismatch between cubic CdZnS and hexagonal $MoSe_2$ contributes to the observed expansion.

Fig. 2(b) displays the wide-scan XPS spectrum, in which distinct signals from cadmium, zinc, sulfur, molybdenum, and selenium, providing direct evidence for the effective incorporation of all elemental components into the 1 T MS/CZS hybrid architecture.

The XRD pattern of 2H-$MoSe_2$ in Fig. 2(c) shows distinct peaks at 13.7° (002), 31.4° (100), and 55.9° (110), indicating a well-crystallized structure. For 1 T/2H-$MoSe_2$, the (002) peak shifts to a lower angle of around 10°, suggesting an expanded interlayer spacing, a hallmark of the distorted octahedral coordination in the 1 T phase [27]. Relative to other structural forms, the 1 T phase features lower crystallographic symmetry, greater structural disorder, and higher electrical conductivity [29]. The broader and less intense diffraction peaks of 1 T/2H-$MoSe_2$ suggest a smaller crystallite size and the presence of a distorted metastable phase.

Raman spectroscopy provided further insight into the vibrational properties and phase characteristics of the composites. In Fig. 2(d), both

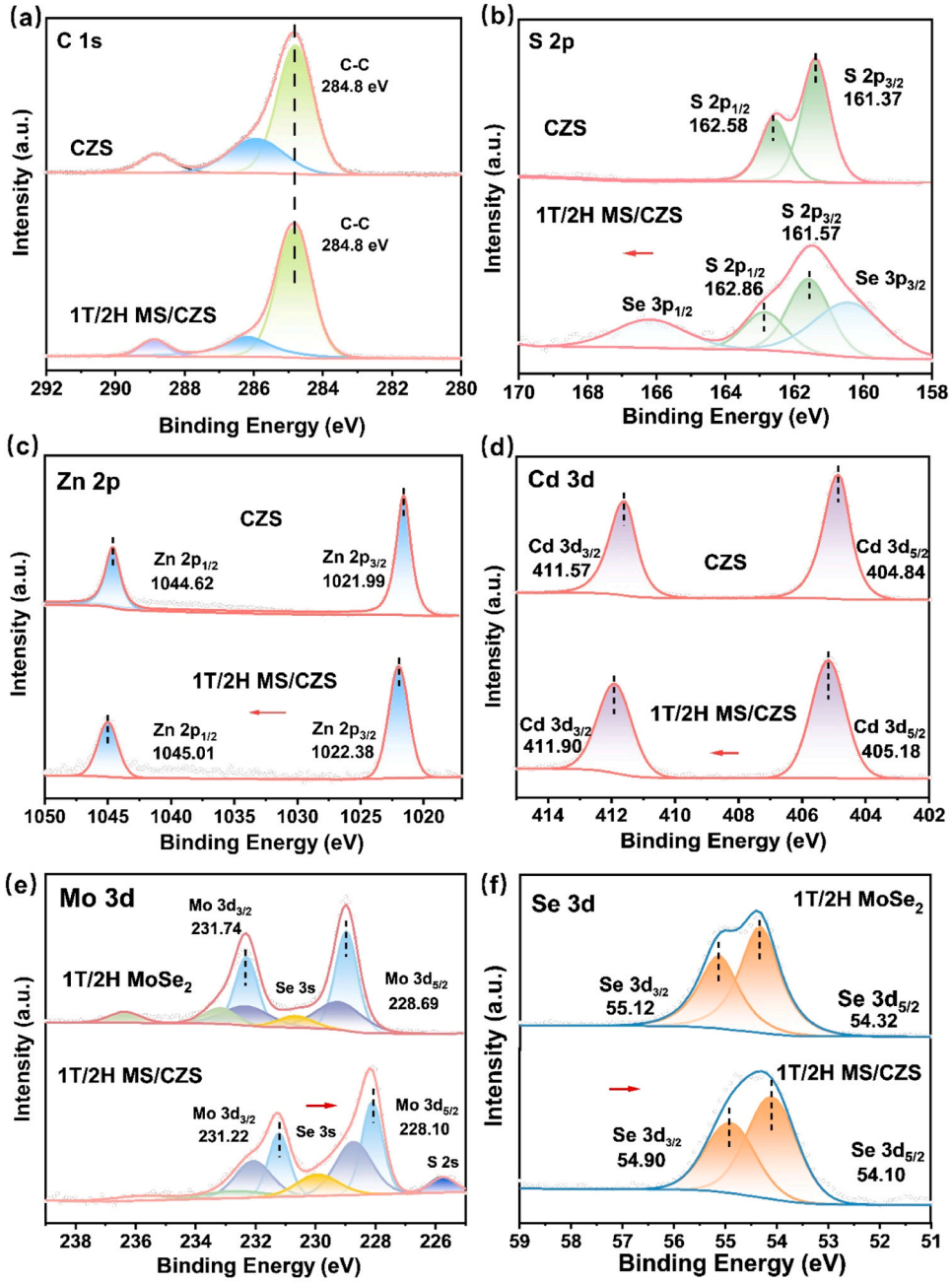

Fig. 3. High-resolution XPS spectra of (a) C 1 s, (b) S 2p, (c) Zn 2p, (d) Cd 3d, (e) Mo 3d, (f) Se 3d.

materials display two dominant vibrational signals at 233.4 cm^{-1} and 283.7 cm^{-1} , attributable to the in-plane E^1_2g and out-of-plane A_1g modes of $MoSe_2$ [30]. The 2H-$MoSe_2$ sample shows sharp and well-defined peaks, indicating high crystalline quality. In contrast, the 1 T/2H-$MoSe_2$ composite exhibits additional peaks at approximately 197 cm^{-1} , 355.6 cm^{-1} , and 489.7 cm^{-1} , which are attributed to J_1, J_2, and J_3 modes typically associated with the 1 T phase [31]. These features suggest lattice distortion and electronic structure modifications in 1T-$MoSe_2$, which may influence its electrical and ionic conductivity, thereby affecting photocatalytic performance [29].

As depicted in Fig. S2, 1 T/2H-MS, 2H-MS, and CdZnS all exhibit type IV isotherms according to nitrogen adsorption–desorption measurements. The BET surface area (S_{BET}) and porosity characteristics of the catalysts are summarized in Table S1. Pure CdZnS exhibits the highest S_{BET} (142.6 m^2/g), while both $MoSe_2$-modified composites show slightly reduced surface areas (106.5–113.5 m^2/g). However, the 1 T/2H-$MoSe_2$/CdZnS sample features the largest pore diameter (18.6 nm) and highest pore volume (0.57 cm^3/g), suggesting a more open and accessible structure. Despite the moderate reduction in surface area, the 1 T/2H-$MoSe_2$/CdZnS demonstrates significantly enhanced photocatalytic activity, indicating that surface area alone does not dictate performance. Rather, the superior H_2 evolution rate is primarily attributed to efficient charge separation and rapid interfacial electron transfer driven by the S-scheme mechanism and the conductive 1 T phase.

Fig. 3 presents the X-ray photoelectron spectroscopy (XPS) analysis of CdZnS (CZS), $MoSe_2$, and the 1 T $MoSe_2$/CdZnS (1 T MS/CZS) composite. The high-resolution S 2p spectrum (Fig. 3(b)) reveals two well-defined features for pristine CdZnS at 161.37 eV and 162.68 eV, assigned to S $2p_{3/2}$ and S $2p_{1/2}$, respectively. In the 1 T MS/CZS composite, these signals shift slightly toward higher binding energies (161.57 eV and 162.86 eV), accompanied by the appearance of a Se 3p

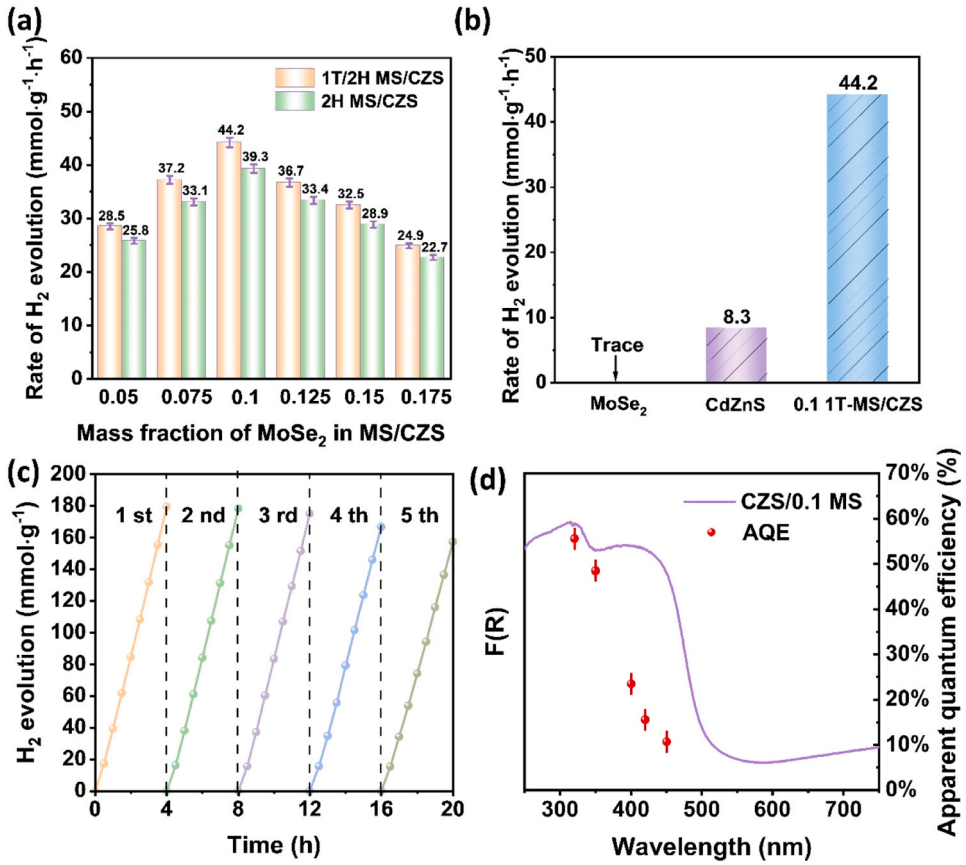

Fig. 4. (a) H_2 production rates of various samples. (b) Photocatalytic performance in H_2 evolution comparing $MoSe_2$, CdZnS, 0.1 1 T/2H-$MoSe_2$/CdZnS, (c) Recycling photocatalytic H_2 production tests over 1 T/2H-$MoSe_2$/CdZnS and (d) UV–Vis DRS and wavelength-dependent AQE of photocatalytic H_2 generation over 1 T/2H-$MoSe_2$/CdZnS.

signal near 162.86 eV. The Zn 2p spectrum (Fig. 3(c)) exhibits binding energies of 1021.99 eV (Zn $2p_{3/2}$) and 1044.92 eV (Zn $2p_{1/2}$) in pure CZS, which shift to 1022.38 eV and 1045.61 eV, respectively, in the composite. Similarly, as shown in Fig. 3(d), the Cd $3d_{5/2}$ and Cd $3d_{3/2}$ peaks are located at 404.84 eV and 411.57 eV, respectively, which undergo a slight positive shift to 405.18 eV and 411.90 eV in 1 T MS/CZS. These consistent positive shifts in the binding energies of S, Zn, and Cd suggest a decreased electron density around these elements in CdZnS [32].

In the high-resolution XPS spectrum of S 2p (Fig. 3(b)), a slight but discernible positive shift (~0.2–0.3 eV) in the binding energy is observed for the 1T-$MoSe_2$/CdZnS composite compared to pure CdZnS. This shift suggests a change in the local chemical environment of sulfur atoms upon heterojunction formation. Specifically, the electron-rich metallic 1T-$MoSe_2$ phase can act as an electron donor toward CdZnS, leading to a partial depletion of electron density around S^{2-} sites in the sulfide lattice. According to the principle of core-level binding energy shifts, a decrease in electron density around an atom results in less effective shielding of the nucleus, thereby increasing the measured binding energy. Alternatively, the shift may also arise from interfacial charge redistribution driven by the formation of a built-in electric field at the 1T-$MoSe_2$/CdZnS interface—consistent with the proposed S-scheme or type-II heterojunction mechanism. Such interfacial electron coupling not only modifies the surface potential but also subtly perturbs the Cd–S or Zn–S bonding states, further contributing to the observed peak shift. This observation aligns well with the enhanced charge separation evidenced by PL quenching, transient photocurrent response, and EIS measurements.

Fig. 3(e) presents the high-resolution XPS spectrum of the Mo 3d region. In the case of pristine 1 T/2H-MS, characteristic peaks corresponding to Mo $3d_{5/2}$ and Mo $d_{3/2}$ are observed at binding energies of 229.69 eV and 232.74 eV, respectively, accompanied by a signal arising from Se 3 s electrons. In the 1 T MS/CZS composite, these peaks shift negatively to 229.88 eV and 231.82 eV, indicating an increase in electron density around the Mo atoms. The Se 3d XPS spectrum is illustrated in Fig. 3(f). For the pristine 1 T/2H-MS sample, the Se $3d_{5/2}$ and Se $3d_{3/2}$ peaks are positioned at 54.32 eV and 55.12 eV, respectively. These peaks shift noticeably to lower binding energies of 54.10 eV and 54.90 eV in the composite [25]. These results collectively demonstrate a significant electronic interaction between CdZnS and $MoSe_2$, suggesting not only a transfer of electrons from CdZnS to $MoSe_2$ but also the electrostatic effects arising from e^- redistribution at the composite interface. Specifically, the $MoSe_2$ surface may serve as an e^- reservoir, enabling efficient capture and accumulation of light-induced e^- under illumination.

3.2. *Activity and stability*

Fig. 4(a) and (b) present a comparative evaluation of the photocatalytic hydrogen evolution rates for pure CdZnS, $MoSe_2$, and a series of x% $MoSe_2$/CdZnS composites with different mass ratios of the two $MoSe_2$ phases were evaluated and compared. With increasing $MoSe_2$ content, the H_2 generation activity of the 1 T/2H $MoSe_2$/CdZnS composites first increased and then decreased. The optimal catalytic activity was achieved at a 10 wt% $MoSe_2$ content, where the enhanced charge transport capability of the 1 T/2H-$MoSe_2$ cocatalyst supports effective dissociation of photoexcited electron–hole pairs. However, excessive $MoSe_2$ may lead to increased charge recombination or blockage of active sites, resulting in reduced activity. The 10 % 1 T/2H MS/CZS sample exhibited the optimal H_2 evolution rate of 44.9 $mmol \cdot g^{-1} \cdot h^{-1}$, marking

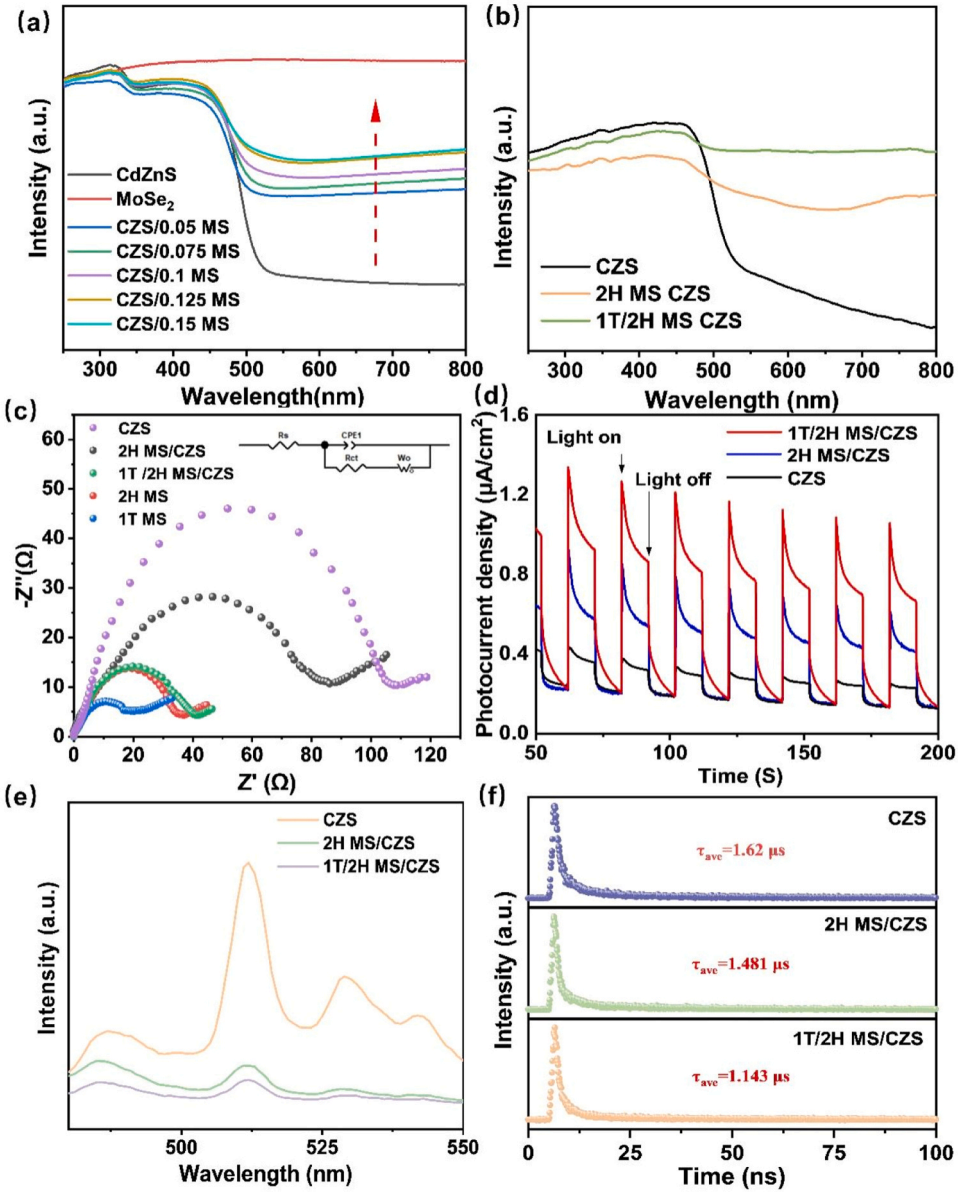

Fig. 5. (a, b) UV-Vis DRS spectra of bare CdZnS, $MoSe_2$, and different samples of 1 T/2H-MS/CZS composites, (c) EIS Nyquist plots for bare CdZnS, $MoSe_2$, and $MoSe_2$/CdZnS composites, (d) Photocurrent responses, (e) Photoluminescence, and (f) TRPL spectra of CdZnS, 2 H MS/CZS, and 1 T/2H-MS/CZS.

a 5.4-fold enhancement compared to pure CdZnS (8.3 mmol·g^{-1}·h^{-1}). To rule out non-photocatalytic contributions, the reaction temperature was monitored under 300 W Xe lamp illumination (with water cooling); the increase was < 3 °C over 4 h, confirming that the enhanced H_2 evolution stems from photocatalysis rather than photothermal effects. To assess the durability as well as structural robustness of the 10 % MS/CdZnS composite, cycling tests were performed. In Fig. 4(c), the 10 % MS/CdZnS remained high activity even over 5 successive cycles, indicating outstanding recyclability and structural robustness. To evaluate the stability of the 1 T/2H-$MoSe_2$/CdZnS composite, the catalyst was recovered after five consecutive H_2 evolution cycles (20 h total irradiation) and characterized by XRD, XPS, and Raman spectroscopy. As shown in Figs. S3–S5, all three techniques reveal negligible changes compared to the fresh sample. The XRD pattern shows no new diffraction peaks or peak shifts, confirming retention of phase purity and crystallinity. XPS survey and high-resolution spectra of Mo 3d, Se 3d, Cd 3d, Zn 2p, and S 2p exhibit no significant shifts in binding energy or changes in peak shape, indicating excellent chemical stability of all components. Similarly, Raman spectra retain the characteristic features of both 1 T and 2 H phases without noticeable intensity variation. Collectively, these results confirm that the heterostructure remains structurally and chemically intact during prolonged photocatalytic operation, likely owing to the efficient S-scheme charge transfer that mitigates photocorrosion of CdZnS. Furthermore, 1 T/2H MS/CZS composite achieved an apparent quantum efficiency (AQE) of 56 % under 320 nm irradiation, as summarized in Fig. 4(d).

3.3. Mechanism and discussion

The optical characteristics of the samples were analyzed using UV-Vis diffuse reflectance spectroscopy. As illustrated in Fig. 5(a), the incorporation of 1 T $MoSe_2$ significantly enhanced the light absorption into the visible region. This improvement arises from the relatively narrow bandgap of $MoSe_2$, which enables efficient visible-light harvesting [33]. Additionally, the creation of a heterostructure at the contact region of CdZnS and 1 T/2H-$MoSe_2$ promotes efficient transfer of photogenerated charges across the boundary, thereby enhancing the overall catalytic activity under illumination. A comparative study of the

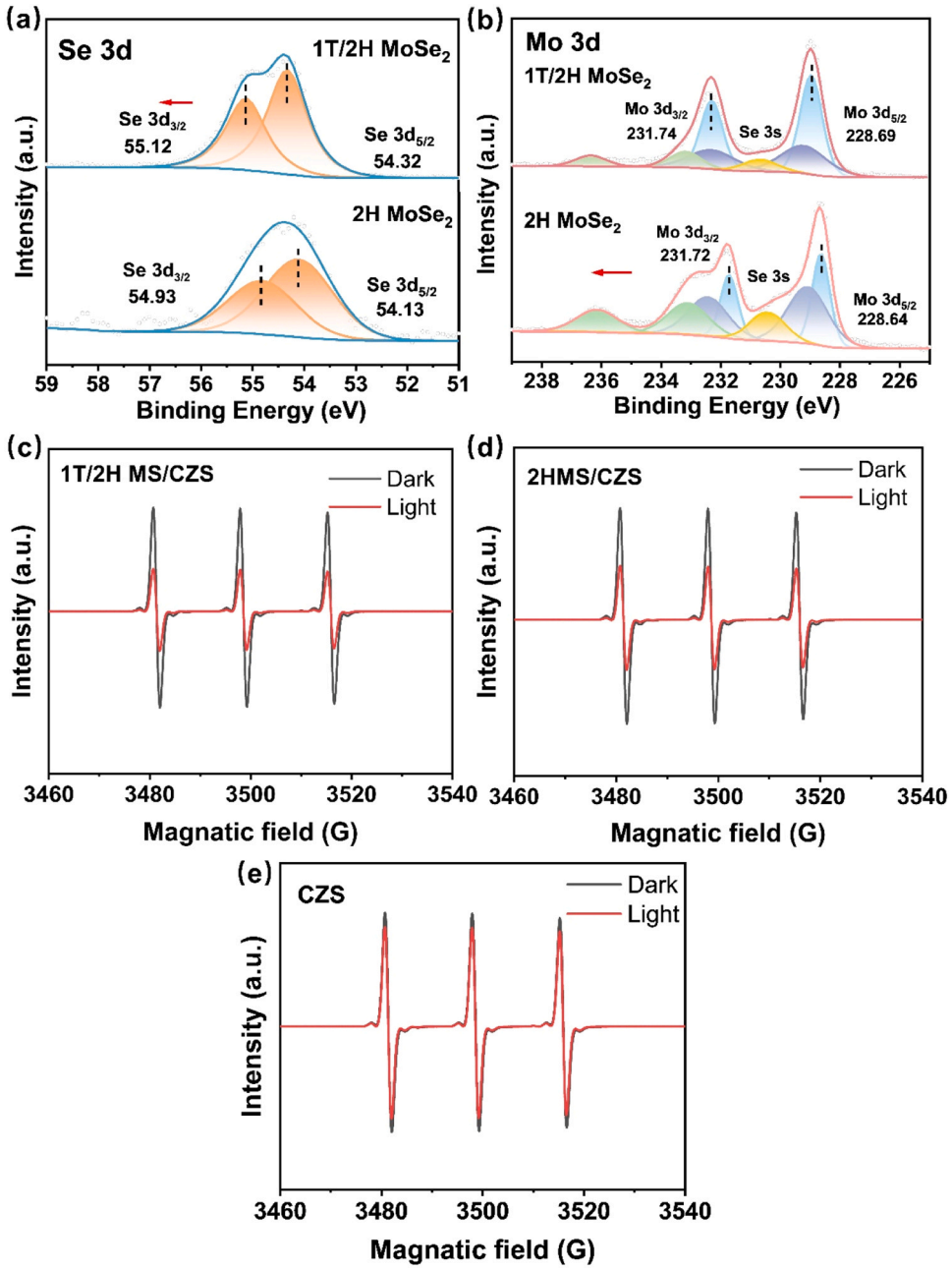

Fig. 6. (a, b) High resolution XPS spectra of Se 3d, Cd 3d in 1 T/2H-MS and 2 H MS, (d-f) EPR spectra of TEMPO.

optical absorption of composites with 1 T and 2 H phases is presented in Fig. 5(b), where 1 T/2H-$MoSe_2$/CdZnS exhibits markedly stronger absorption than its 2 H counterpart. Metallic 1T-$MoSe_2$ exhibits stronger visible-light absorption and higher activity than semiconducting 2H-$MoSe_2$, due to its narrower bandgap [33], superior charge transfer, and higher carrier density, which collectively enhance photocatalytic performance.

Electrochemical impedance spectroscopy (EIS) was carried out under visible-light irradiation to evaluate interfacial charge transfer dynamics across the electrode/electrolyte interface. As shown in the Nyquist plots (Fig. 5(c)), all samples exhibit a single semicircular arc in the high-to-medium frequency region, followed by a low-frequency linear tail. The arc diameter is governed by the charge transfer resistance (Rct), which inversely correlates with interfacial electron transfer efficiency—smaller arcs indicate lower Rct and more efficient charge separation and transport. The observed trend follows the order: 1T-$MoSe_2$ < 2H-$MoSe_2$ < 1 T/2H-$MoSe_2$/CdZnS < 2H-$MoSe_2$/CdZnS < CdZnS, with 1T-$MoSe_2$ displaying the smallest arc due to its metallic nature and high electrical conductivity. In contrast, pure CdZnS exhibits the largest arc, reflecting bulk/surface recombination and sluggish interfacial kinetics. The decrease in Rct upon coupling CdZnS with $MoSe_2$ suggests the beneficial role of $MoSe_2$ in promoting carrier separation. The low-frequency linear tail, present in all spectra, is characteristic of Warburg diffusion impedance (Wo), arising from ion migration (e.g., H^+ or sacrificial agent species) in the electrolyte. In accordance with the data presented in Fig. 5(d), the material incorporating the 1 T composite also demonstrates a significantly stronger photocurrent response, suggesting more efficient separation of photogenerated charge carriers. Photoluminescence (PL) spectra presented in Fig. 5(e) reveal a significant reduction in emission intensity for 1 T/2H-$MoSe_2$/CdZnS compared to pure CdZnS, indicating suppressed electron-hole recombination as a result of incorporating 1 T/2H-$MoSe_2$. To quantitatively evaluate the

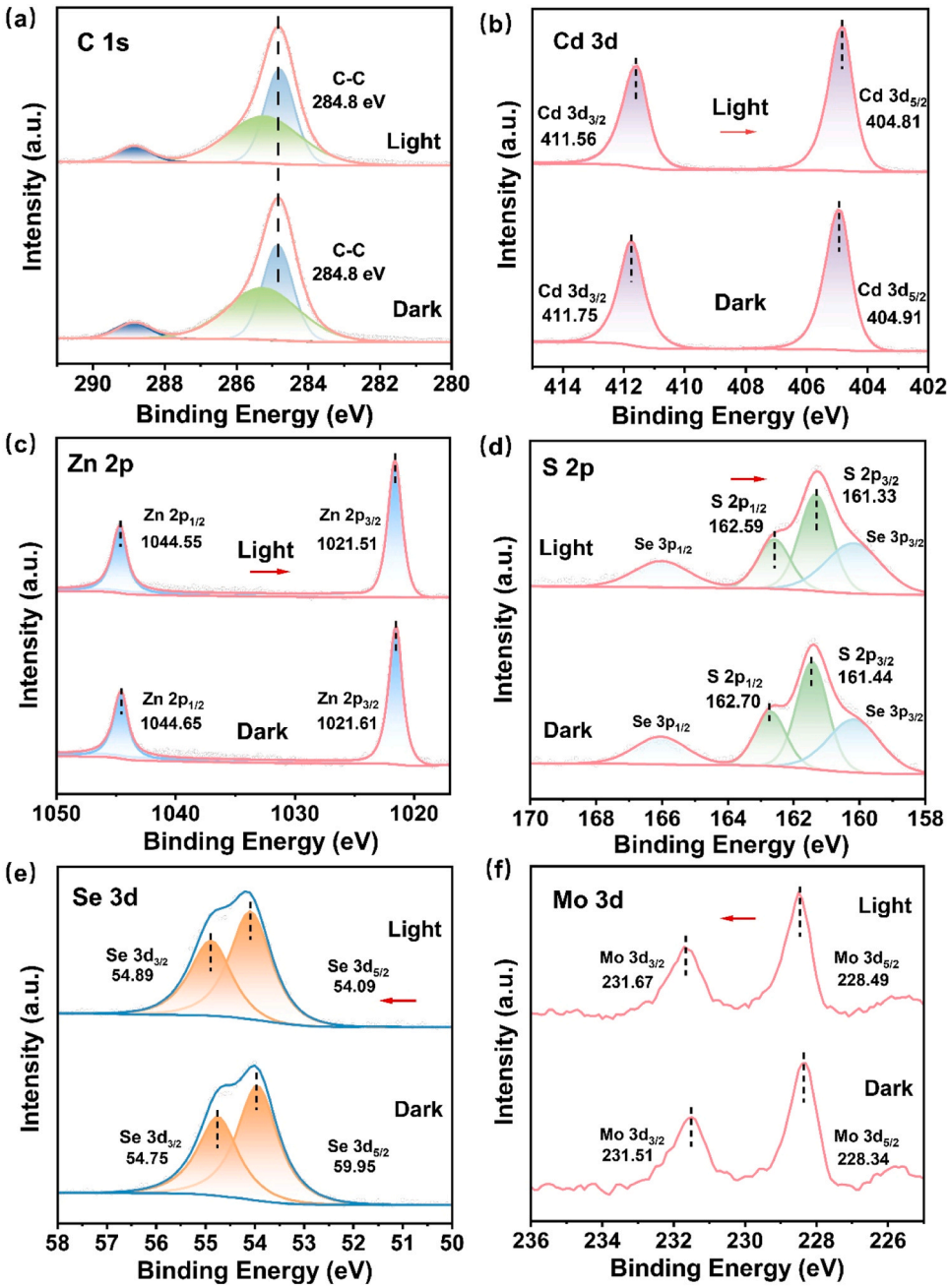

Fig. 7. High-resolution in-situ XPS spectra of (a) C 1 s, (b) Cd 3d, (c) Zn 2p, (d) S 2p, (e)Se 3d, and (f) Mo 3d of 1 T/2H-$MoSe_2$/CdZnS.

charge carrier dynamics, the time-resolved photoluminescence (TRPL) decay curves in Fig. 5(f) were fitted using a bi-exponential function:

$$I(t) = A_1 \exp\left(-\frac{t}{\tau_1}\right) + A_2 \exp\left(-\frac{t}{\tau_2}\right)$$

where $I(t)$ is the PL intensity at time t, A_1 and A_2 are the pre-exponential factors, and τ_1 and τ_2 represent the short-and long-lived lifetime components. The average fluorescence lifetime (τ_{avg}) was calculated according to:

$$\tau_{avg} = \frac{A_1\tau_1^2 + A_2\tau_2^2}{A_1\tau_1 + A_2\tau_2}$$

The average fluorescence lifetime of 1 T/2H-$MoSe_2$/CdZnS (τ_{ave} = 1.143 μs) is considerably shorter than that of pure CdZnS (τ_{ave} = 1.62 μs) and 2H-$MoSe_2$/CdZnS (τ_{ave} = 1.481 μs). The parameter is provided in Table S2. In composite photocatalysts, a shorter carrier lifetime typically signals enhanced interfacial charge transfer, not detrimental recombination. In heterostructures for photocatalytic water splitting, this reduction arises from efficient charge separation across the interface, where one component rapidly extracts carriers from the other. This process suppresses recombination and quenches photoluminescence. Materials like $MoSe_2$ further introduce non-radiative pathways that accelerate surface charge transfer for redox reactions. Although these mechanisms shorten the observed lifetime, they significantly boost photocatalytic activity. Thus, efficient interfacial charge separation is key to high performance.

High-resolution XPS profiles of the Se 3d and Mo 3d core levels for the 1 T and 2 H phases of $MoSe_2$ are compared in Fig. 6(a) and (b). In the Se 3d region, the binding energies of the Se $3d_{5/2}$ and Se $3d_{3/2}$ in 1 T/2H-$MoSe_2$ were observed at 55.12 eV and 54.32 eV, respectively, which are 0.19 eV higher than those of 2H-$MoSe_2$ (54.93 eV and 54.13 eV). For

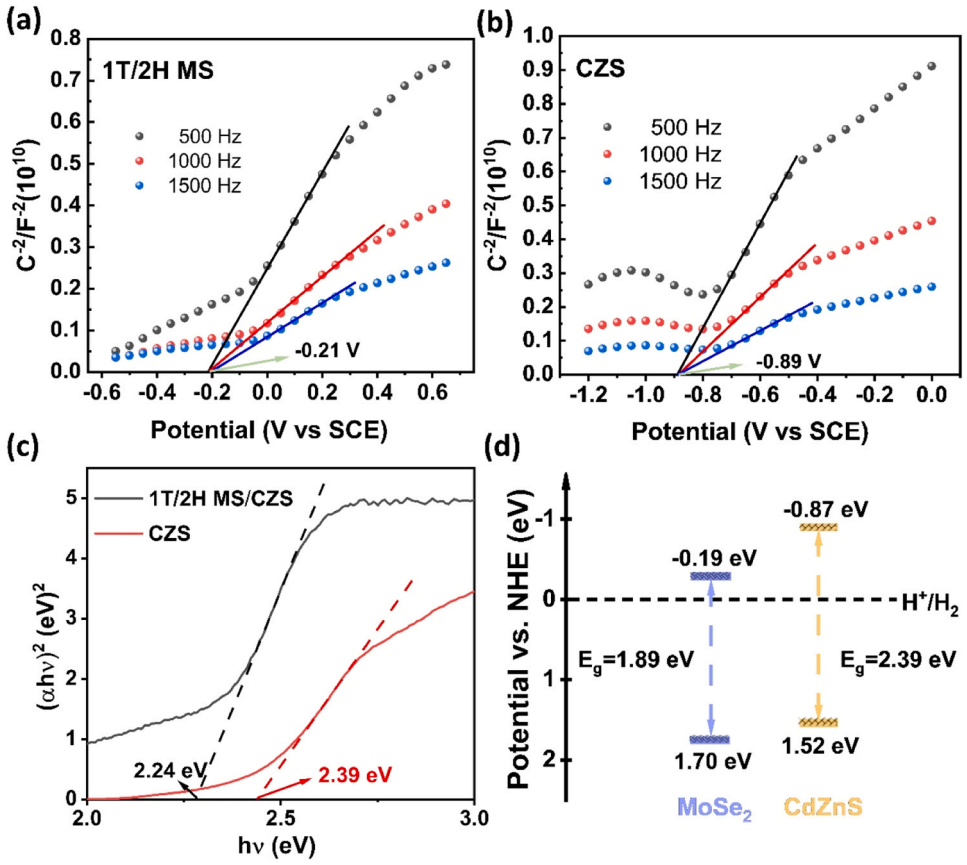

Fig. 8. (a, b) Mott-Schottky plots of 1 T/2H MS and CdZnS, (c)Tauc plots of the UV–Vis spectra of CdZnS and 1 T/2H MS, (d) Schematic illustration of the band structure of CdZnS and 1 T/2H MS.

the Mo 3d spectra, the binding energies for Mo $3d_{5/2}$ and Mo $3d_{3/2}$ appeared at 231.74 eV and 228.61 eV in 1 T/2H-$MoSe_2$, while those of 2H-$MoSe_2$ are positioned at 231.72 eV and 228.64 eV, resulting in a negligible difference of only 0.02 eV in the Mo $3d_{3/2}$ position. The Se 3 s peak followed a similar trend, with slightly higher binding energies in the 1 T phase. The observed binding energy shifts originate from differences in crystal structure and electronic interactions. In 2H-$MoSe_2$, Mo atoms are in trigonal prismatic coordination with Se arranged in an octahedral symmetry, where covalent bonding dominates, and electron density is uniformly distributed [34]. In contrast, 1T-$MoSe_2$ adopts a distorted octahedral structure with shortened Mo–Se bonds, enhanced covalency, and localized charge rearrangement. This leads to an increased effective nuclear charge around Se atoms and consequently higher binding energies [35]. Although the 1 T phase exhibits a trigonal crystal system with shorter Mo–Mo bonds and coordination distortion, while the 2 H counterpart forms a hexagonal arrangement with longer Mo–Mo bonds and higher stacking order, both phases maintain Mo^{4+} and Se^{2-} oxidation states without detectable deviation or impurity-related peaks, confirming high sample purity and structural stability.

Fig. 6(d-f) present the electron paramagnetic resonance (EPR) signals of 1 T/2H-MS/CZS, 2H-MS/CZS, and pure CdZnS using TEMPO as a probe molecule under both light-off and light-on conditions. In the absence of light, all samples exhibited similar EPR signal intensities, indicating negligible generation of reducing electrons without photoexcitation. Under light irradiation, however, a marked decrease in EPR signal intensity was observed for the 1 T/2H MS/CZS sample in contrast to both the 2 H MS/CZS and pristine CdZnS. This significant signal suppression indicates enhanced generation of photoinduced electrons in the 1 T/2H-MS/CZS composite, which are rapidly scavenged by TEMPO to form TEMPOH, thereby reducing the EPR signal. The diminished EPR response not only reflects enhanced electron generation and trapping under illumination but also confirms the superior electron-producing capability of the 1 T/2H-MS/CZS composite.

Fig. 7 presents a comparative analysis of the in situ XPS spectra for each element in the $MoSe_2$/CdZnS composite under dark and illuminated conditions. Light irradiation induced systematic shifts in the binding energies of all elements. The peaks of Cd $3d_{5/2}$ and Cd $3d_{3/2}$ shifted negatively from 411.75 eV and 404.91 eV to 411.56 eV and 404.81 eV, respectively. Zn $2p_{1/2}$ and Zn $2p_{3/2}$ shifted from 1044.65 eV and 1021.61 eV to 1044.55 eV and 1021.51 eV. The S $2p_{3/2}$ and S $2p_{1/2}$ binding energies also reduced, shifting from 161.44 eV and 162.70 eV to 161.33 eV and 162.59 eV. In contrast, the Se $3d_{5/2}$ and Se $3d_{3/2}$ peaks showed a positive shift, increasing from 54.75 eV and 59.95 eV to 54.89 eV and 61.33 eV, while the Mo $3d_{5/2}$ and Mo $3d_{3/2}$ rose from 231.51 eV and 228.34 eV to 231.67 eV and 228.49 eV, respectively. These consistent shifts indicate that under light illumination, electrons excited into the conduction band of $MoSe_2$ migrate through the heterointerface and subsequently are annihilated by vacancies in the valence band of CdZnS. This results in a decreased electron density around Mo and Se atoms (increased binding energy values), whereas the electron density at Cd, Zn, and S sites rises (decreased binding energy values) [36]. This process suggests the formation of efficient spatial separation of carriers across the heterojunction, which plays a critical role in minimizing electron–hole recombination as well as extending the lifetime of photogenerated charges [37].

The charge transfer behavior and photocatalytic mechanism of the heterojunction system are illustrated in Fig. 8. As evidenced by the Mott–Schottky plots in Fig. 8(a), both CdZnS and 1 T/2H-$MoSe_2$ measured at 500, 1000, and 1500 Hz exhibit positive slopes, verifying their n-type semiconducting nature. The flat-band potentials, determined by extrapolating the linear regions in Fig. 8(b), are –0.21 V (*vs.*

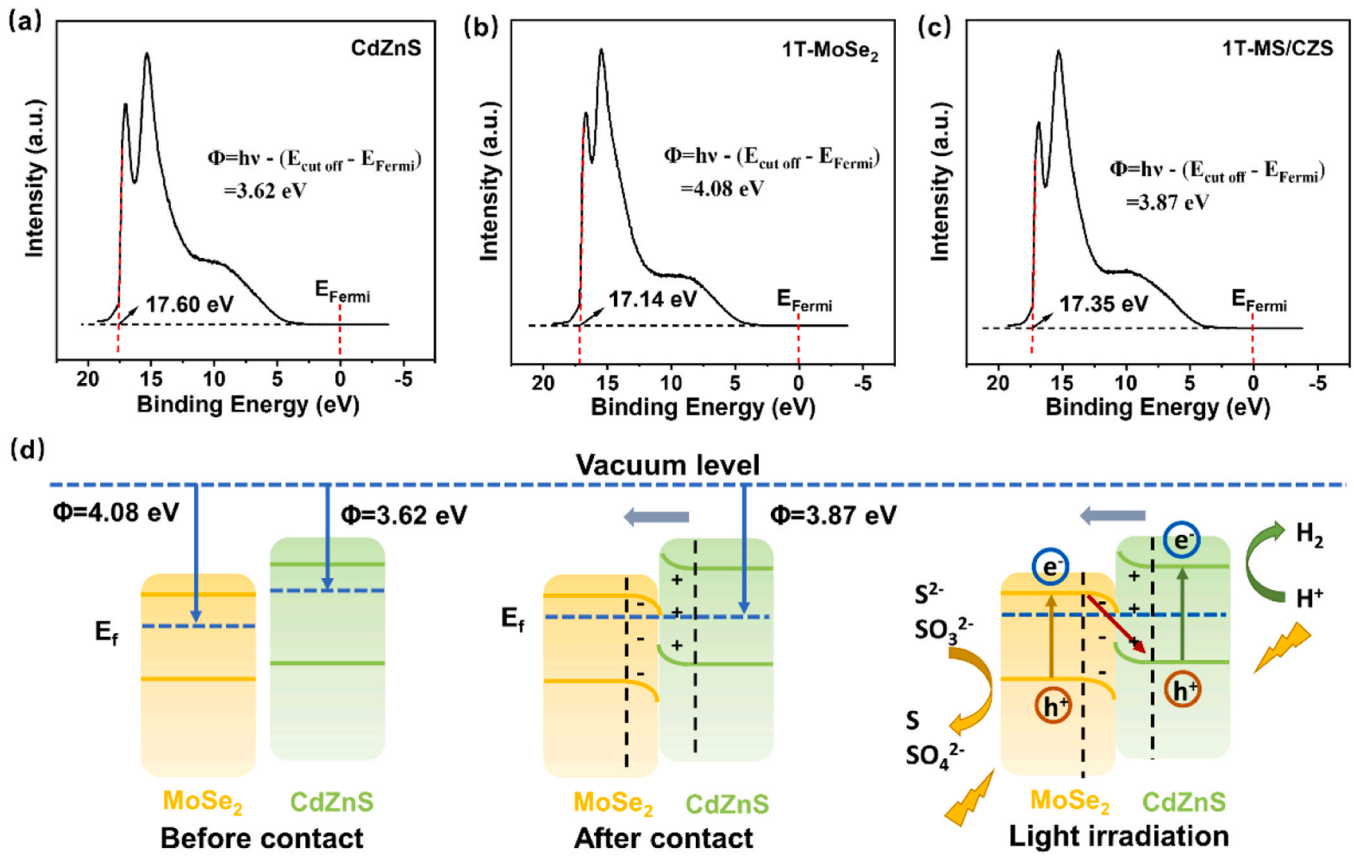

Fig. 9. UPS spectrum of (a) CdZnS, (b) 1 T/2H-$MoSe_2$, (c) 1 T/2H-$MoSe_2$/CdZnS, and (d) Schematic illustration of band positions for CdSe, MXene and, 1 T/2H-$MoSe_2$/CdZnS.

SCE) for CdZnS and –0.89 V (*vs. SCE*) for 1 T/2H-$MoSe_2$. For n-type semiconductors, the conduction band edge potential is typically approximately 0.2 V more negative than the flat-band potential. Based on the equation:

$$E_{CB} \approx E_{fb} - 0.20 \quad V$$

the flat-band potentials of the various samples were calculated to be −0.41 V (vs. *SCE*) and −1.09 V (*vs. SCE*). We explicitly stated in this work that all potentials were converted to the Normal Hydrogen Electrode (NHE) scale using the equation:

$$E_{NHE} = E_{SCE} + 0.22 \quad V$$

Based on the equation, the flat-band potentials of the samples were determined to be −0.19 V (*vs. NHE*) and −0.87 V (*vs. NHE*). The optical band gaps, derived from Tauc plots (Fig. 8(c)), are approximately 2.24 eV for 1 T/2H-$MoSe_2$/CdZnS and 2.39 eV for CdZnS. By combining the Mott–Schottky and Tauc plot results, the band alignment of the two materials is constructed. As illustrated in Fig. 8(d), the conduction band (CB) of CdZnS is located at −0.87 V (*vs. NHE*), whereas the valence band (VB) edge is situated at 1.52 eV (*vs. NHE*), yielding a band gap of 2.39 eV. In comparison, 1 T/2H-$MoSe_2$ shows a CB position of −0.19 V, a VB position at 1.70 eV, and a band gap of 1.89 eV, respectively [36, 38]. This distinct band alignment facilitates the construction of a heterojunction with efficient charge separation. Based on these findings, an S-scheme heterojunction is proposed between CdZnS and 1T-$MoSe_2$ under light irradiation. The more negative CB of CdZnS allows accumulation of photogenerated electrons for the water reduction reaction (hydrogen evolution), while the more positive VB of 1 T/2H-$MoSe_2$ promotes hole gathering and enhances the water oxidation reaction. This well-matched band structure effectively drives spatial charge migration, suppresses the annihilation of e^- and hole, which markedly enhances the material's ability to produce hydrogen under light irradiation.

The work functions of the synthesized samples were measured using ultraviolet photoelectron spectroscopy (UPS). Fig. 9 displays the UPS results and corresponding band alignment diagrams for CdZnS, 1 T/2H-$MoSe_2$, and their hybrid structure. Analyzing the secondary electron cutoff and Fermi edge positions, the work function (Φ) of each component was accurately calculated, providing insights into the band structure modulation upon heterojunction formation. Fig. 9(a) displays the secondary electron cutoff of CdZnS is observed at 17.60 eV. The work function value of 3.62 eV was derived from the He I radiation photon energy ($h\nu = 21.22$ eV) and the position of the Fermi edge. For 1 T/2H-$MoSe_2$ (Fig. 9(b)), the cutoff appears at 17.14 eV, corresponding to a work function of 4.08 eV—higher than that of CdZnS, indicating stronger electron affinity. The UPS spectrum of the 1 T/2H-MS/CZS composite (Fig. 9(c)) shows a cutoff at 17.35 eV, yielding a work function of 3.87 eV. This intermediate value suggests significant electron redistribution and interfacial charge transfer during heterojunction formation.

Fig. 9(d) illustrates the band alignment before and after contact between CdZnS and 1 T/2H-$MoSe_2$ and the electron transfer mechanism under illumination. Upon light irradiation, both CdZnS and 1 T/2H-$MoSe_2$ are photoexcited, generating electron-hole pairs in their respective conduction bands (CB) and valence bands (VB). However, owing to the disparity in work function—3.62 eV for CdZnS and 4.08 eV for 1 T/2H-$MoSe_2$—electrons spontaneously transfer from CdZnS to $MoSe_2$ upon contact, resulting in Fermi level alignment and the formation of a built-in electric field. This results in bending upward in CdZnS and downward in $MoSe_2$. This internal potential gradient functions as a motivating force for unidirectional carrier migration.

The built-in potential gradient drives electrons, generated under

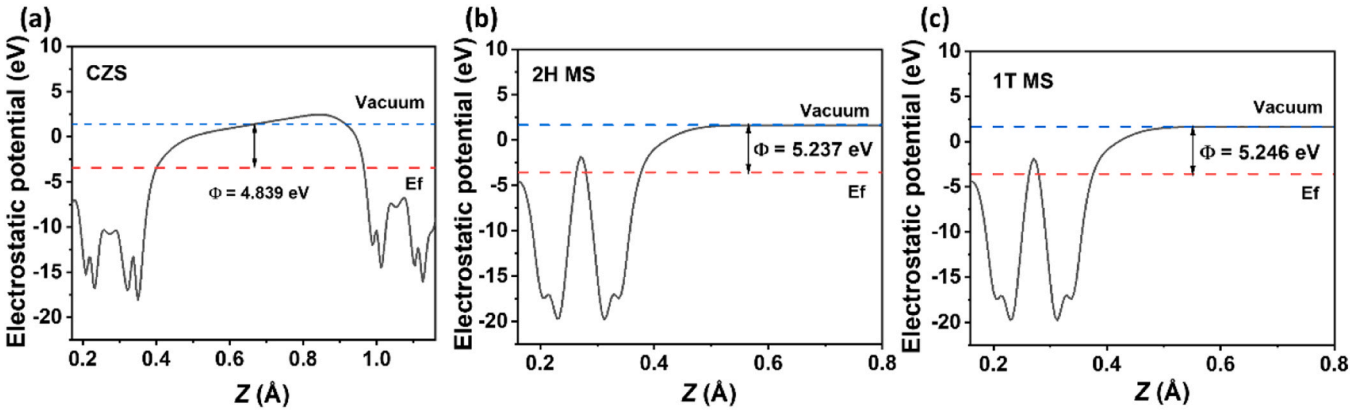

Fig. 10. Electrostatic potentials of the (a) CdZnS, (b) 2 H MS, and (c) 1 T/2H-MS.

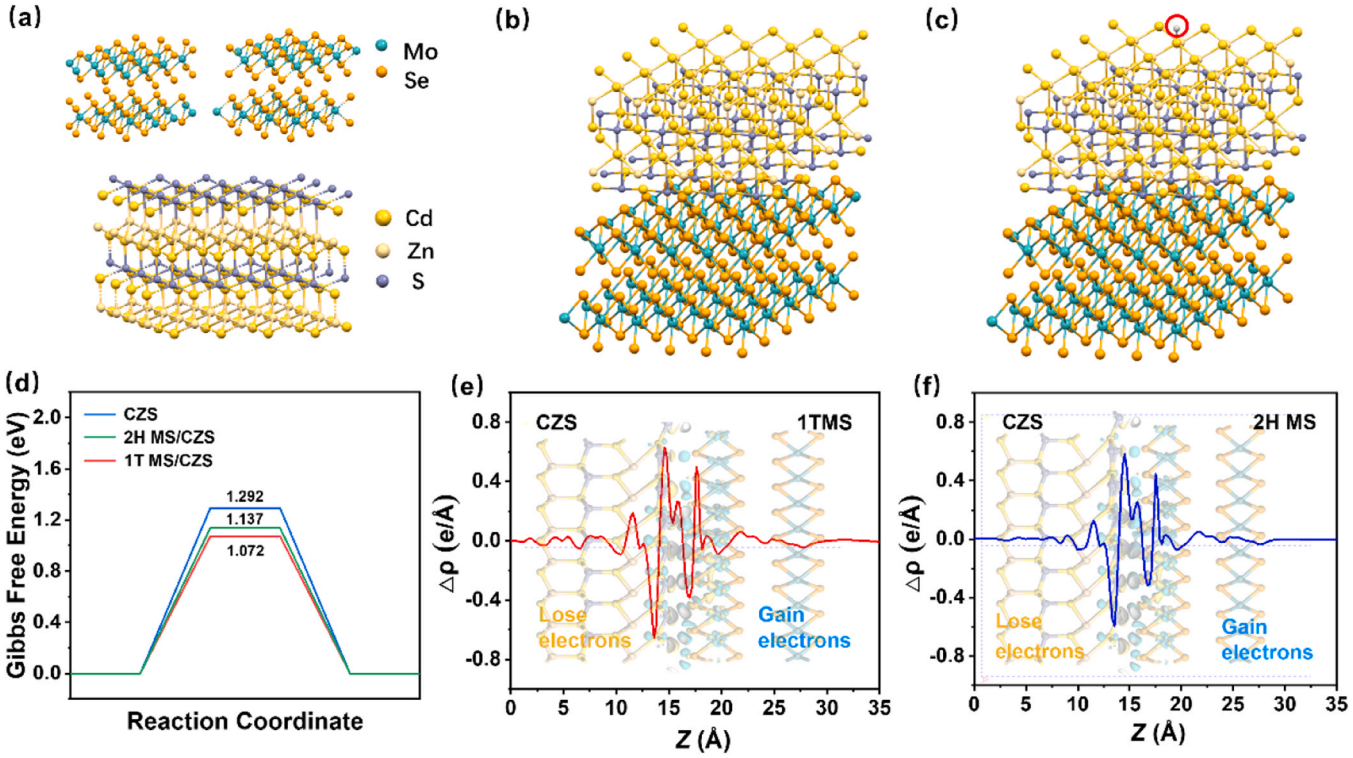

Fig. 11. (a-c) Schematic structure models of H adsorption of 1 T/2H-MS/CZS, (d) Free energy diagrams of reaction of CdZnS, 2 H MS/CZS, and 1 T/2H-MS/CZS, (e, f) Charge density difference and Planar-averaged electron density difference along with Z direction of 1 T/2H-MS/CZS and 2H-MS/CZS.

illumination, from the CB of $MoSe_2$ toward the interfacial region, while the charge carriers in the VB of CdZnS simultaneously migrate in an identical direction. These less-reductive electrons and less-oxidative holes undergo efficient recombination at the heterojunction interface, effectively eliminating the lower-energy charge carriers. As a result, the highly energetic electrons are preserved in the CB of CdZnS, whereas the more reactive charge vacancies accumulated in the VB of $MoSe_2$ are spatially separated, enabling robust redox reactions.

This charge transfer pathway is characteristic of a direct S-scheme mechanism. The confinement of charge carriers within the more negative CB of CdZnS enables efficient hydrogen evolution via proton reduction, while the presence of charge carriers in the more positive VB of $MoSe_2$ facilitates oxidative reactions. The proposed mechanism is further supported by in-situ XPS analysis (Fig. 7), which shows that the Cd 3d and Zn 2p peaks exhibit a negative shift of 0.1–0.2 eV, while the Mo 3d and Se 3d peaks show a positive shift of 0.1–0.2 eV under light irradiation. These opposing binding energy shifts provide direct evidence of spatially separated electron–hole migration across the heterojunction. Collectively, these findings reveal that the 1 T/2H-MS/CZS heterojunction establishes an efficient S-scheme charge transfer pathway that enhances spatial charge separation, suppresses bulk recombination, and significantly boosts photocatalytic performance.

A comparative study of the electronic structures and H_2 adsorption behaviors of CZS, 2H-$MoSe_2$, and 1 T/2H-MS/CZS was conducted using density functional theory (DFT) calculations. Work function analysis (Fig. 10(a–c)) reveals values of 4.839 eV for CZS, 5.237 eV for 2H-$MoSe_2$, and 5.246 eV for 1 T/2H-$MoSe_2$, indicating that both $MoSe_2$ phases exhibit high electron affinity and can serve as electron acceptors in the heterojunction to facilitate interfacial charge separation.

As illustrated in the structural models (Fig. 11(a–c)), 1 T/2H-$MoSe_2$ contains more lattice distortions and defects, which provide abundant active sites for hydrogen adsorption. In Fig. 11(d), the calculated

hydrogen adsorption free energy (ΔG_H^*) values are 1.292 eV for CZS, 1.137 eV for 2H-MS, and 1.072 eV for 1 T/2H-MS/CZS. The ΔG_H^* of 1 T/2H-MS/CZS is closest to the ideal value, suggesting optimal hydrogen adsorption–desorption equilibrium and enhanced catalytic activity. Charge distribution analysis (Fig. 11(e, f)) further confirms efficient electron transfer at the 1 T/2H-$MoSe_2$/CZS interface, which significantly promotes the hydrogen adsorption process. The 1 T/2H-$MoSe_2$/CZS composite demonstrates certain metallic features (DOS, Fig. S8), with a notably higher charge density near the Fermi level, surpassing that observed in pure CdZnS and $MoSe_2$ phases. Introducing the 1 T/2H-$MoSe_2$ substantially boosts the system's electronic density of states, thereby creating more favorable conditions for effective solar-driven H_2 generation. Collectively, these observations confirm 1 T/2H-MS/CZS hybrid exhibits markedly enhanced efficacy for promoting the H_2 evolution process due to its optimized electronic structure, lower hydrogen adsorption free energy, and efficient interfacial charge transfer.

4. Conclusion

This work describes the successful fabrication of a range of 1 T/2H-MS/CZS hybrids via a precisely regulated hydrothermal approach, and their H_2 evolution capability was systematically investigated. The integration of metallic 1 T/2H-MS significantly enhances the H_2 production activity compared to semiconducting 2H-$MoSe_2$ and pure CdZnS. The optimal composite with 10 wt% 1 T/2H-$MoSe_2$ exhibits a H_2 production rate of 44.9 $mmol \cdot g^{-1} \cdot h^{-1}$, marking a 5.4 times improvement compared to bare CdZnS. Multiple characterization techniques confirm that the superior performance originates from the unique properties of the metallic 1 T/2H-$MoSe_2$ phase, which exhibits enhanced electron transport capability, a narrower bandgap, and a greater density of accessible catalytic centers, collectively enhancing visible-light absorption and facilitating the migration and utilization of photogenerated charges. A charge transfer mechanism following the S-scheme principle is established at the interface of CdZnS and 1 T/2H-$MoSe_2$, promoting the physical isolation of photoinduced electrons and holes, thereby suppressing recombination. DFT calculations reveal that the 1 T/2H-$MoSe_2$/CdZnS interface exhibits optimized free energy for H adsorption ($\Delta G_H^* = 1.072$ eV) and enhanced electron concentration near the Fermi level, both of which act cooperatively to boost the effectiveness of proton reduction for H_2 generation. This study emphasizes the key importance of manipulating crystal phases to regulate the electronic properties and catalytic performance of cocatalysts based on $MoSe_2$. The findings offer valuable understanding for developing high-performance photocatalysts that do not rely on precious metals via crystal phase manipulation and heterojunction construction for sustainable solar energy conversion.

CRediT authorship contribution statement

Yuchen Wei: Formal analysis. **Quanmei Zhou:** Validation. **Wei-Lin Dai:** Writing – review & editing, Visualization, Supervision, Project administration, Funding acquisition. **Linlin Gao:** Writing – original draft, Validation, Investigation. **Jiayi Meng:** Formal analysis. **Yamei Huang:** Methodology, Conceptualization. **Zizheng Wang:** Writing – review & editing. **Yifan Liao:** Investigation.

Declaration of Competing Interest

The authors declare no competing financial interest.

Acknowledgements

This work was funded by the National Key Research and Development Program of China (2021YFA1501404), Natural Science Foundation of Shanghai (22ZR1404200), and the Science and Technology Commission of Shanghai Municipality (2024ZDSYS02).

Appendix A. Supporting information

Supplementary data associated with this article can be found in the online version at doi:10.1016/j.jece.2026.121561.

Data availability

Data will be made available on request.

References

[1] K.K. Mandari, R.R. Eragari, M. Kang, Ag/$AgVO_3$/g-C_3N_4 ternary nanocomposites for enhanced photo- and electrocatalytic hydrogen evolution: synergistic charge separation and interfacial engineering, ACS Appl. Energy Mater. 8 (21) (2025) 16352–16363, https://doi.org/10.1021/acsaem.5c03026.
[2] T. Hisatomi, K. Domen, Reaction systems for solar hydrogen production via water splitting with particulate semiconductor photocatalysts, Nat. Catal. 2 (5) (2019) 387–399, https://doi.org/10.1038/s41929-019-0242-6.
[3] T. Takata, J. Jiang, Y. Sakata, M. Nakabayashi, N. Shibata, V. Nandal, K. Seki, T. Hisatomi, K. Domen, Photocatalytic water splitting with a quantum efficiency of almost unity, Nature 581 (7809) (2020) 411–414, https://doi.org/10.1038/s41586-020-2278-9.
[4] M. Shi, X. Wu, Y. Zhao, R. Li, C. Li, Unlocking the key to photocatalytic hydrogen production using electronic mediators for Z-Scheme water splitting, J. Am. Chem. Soc. 147 (4) (2025) 3641–3649, https://doi.org/10.1021/jacs.4c15540.
[5] J. Ran, H. Zhang, S. Fu, M. Jaroniec, J. Shan, B. Xia, Y. Qu, J. Qu, S. Chen, L. Song, J.M. Cairney, L. Jing, S.-Z. Qiao, $NiPS_3$ ultrathin nanosheets as versatile platform advancing highly active photocatalytic H_2 production, Nat. Commun. 13 (1) (2022) 4600, https://doi.org/10.1038/s41467-022-32256-6.
[6] J. Kosco, S. Gonzalez-Carrero, C.T. Howells, T. Fei, Y. Dong, R. Sougrat, G. T. Harrison, Y. Firdaus, R. Sheelamanthula, B. Purushothaman, F. Moruzzi, W. Xu, L. Zhao, A. Basu, S. De Wolf, T.D. Anthopoulos, J.R. Durrant, I. McCulloch, Generation of long-lived charges in organic semiconductor heterojunction nanoparticles for efficient photocatalytic hydrogen evolution, Nat. Energy 7 (4) (2022) 340–351, https://doi.org/10.1038/s41560-022-00990-2.
[7] J. Liu, Y. Liu, N. Liu, Y. Han, X. Zhang, H. Huang, Y. Lifshitz, S.-T. Lee, J. Zhong, Z. Kang, Metal-free efficient photocatalyst for stable visible water splitting via a two-electron pathway, Science 347 (6225) (2015) 970–974, https://doi.org/10.1126/science.aaa3145.
[8] Z. Li, W. Huang, J. Liu, K. Lv, Q. Li, Embedding CdS@Au into ultrathin $Ti_{3-x}C_2Ty$ to build dual schottky barriers for photocatalytic H_2 production, ACS Catal. 11 (14) (2021) 8510–8520, https://doi.org/10.1021/acscatal.1c02018.
[9] X. Wang, B. Liu, S. Ma, Y. Zhang, L. Wang, G. Zhu, W. Huang, S. Wang, Induced dipole moments in amorphous ZnCdS catalysts facilitate photocatalytic H_2 evolution, Nat. Commun. 15 (1) (2024) 2600, https://doi.org/10.1038/s41467-024-47022-z.
[10] J. Wang, X. Niu, R. Wang, K. Zhang, X. Shi, H.Y. Yang, J. Ye, Y. Wu, High-entropy alloy-enhanced ZnCdS nanostructure photocatalysts for hydrogen production, Appl. Catal. B 362 (2025) 124763, https://doi.org/10.1016/j.apcatb.2024.124763.
[11] Y. Liu, X. Ma, X. Jiang, Z. Jin, Phosphorus-modified two-dimensional graphdiyne (C_nH_{2n-2})/ZnCdS forms S-scheme heterojunctions for photocatalytic hydrogen production, Nanoscale 14 (33) (2022) 12077–12089, https://doi.org/10.1039/D2NR02671F.
[12] J. Zhang, S. Yuan, J. Lin, $Cd_{1-x}Zn_xS$ nanorod solid solutions with sulfur vacancies as effective electron traps for highly efficient photocatalytic hydrogen evolution, J. Phys. Chem. C. 125 (46) (2021) 25600–25607, https://doi.org/10.1021/acs.jpcc.1c08457.
[13] X. Hao, D. Xiang, Z. Jin, Zn-vacancy engineered S-scheme ZnCdS/ZnS photocatalyst for highly efficient photocatalytic H_2 evolution, ChemCatChem 13 (22) (2021) 4738–4750, https://doi.org/10.1002/cctc.202100994.
[14] Z. Li, M. Li, M. Ding, X. Lyu, J. Nie, Z. Jin, Nitrogen-doped biochar assists rapid electron transfer at the ZnCdS/$CoMoO_4$ interface to enhance photocatalytic hydrogen production, J. Colloid Interface Sci. 699 (2025) 138231, https://doi.org/10.1016/j.jcis.2025.138231.
[15] H. Yang, J. Tang, Y. Luo, X. Zhan, Z. Liang, L. Jiang, H. Hou, W. Yang, MOFs-derived fusiform In_2O_3 mesoporous nanorods anchored with ultrafine CdZnS nanoparticles for boosting visible-light photocatalytic hydrogen evolution, Small 17 (36) (2021) 2102307, https://doi.org/10.1002/smll.202102307.
[16] A. Iwase, Y.H. Ng, Y. Ishiguro, A. Kudo, R. Amal, Reduced graphene oxide as a solid-state electron mediator in Z-scheme photocatalytic water splitting under visible light, J. Am. Chem. Soc. 133 (29) (2011) 11054–11057, https://doi.org/10.1021/ja203296z.
[17] S. Manzeli, D. Ovchinnikov, D. Pasquier, O.V. Yazyev, A. Kis, 2D transition metal dichalcogenides, Nat. Rev. Mater. 2 (8) (2017) 17033, https://doi.org/10.1038/natrevmats.2017.33.
[18] R. Yang, Y. Fan, Y. Zhang, L. Mei, R. Zhu, J. Qin, J. Hu, Z. Chen, Y. Hau Ng, D. Voiry, S. Li, Q. Lu, Q. Wang, J.C. Yu, Z. Zeng, 2D transition metal dichalcogenides for photocatalysis, Angew. Chem. Int. Ed. 62 (13) (2023) e202218016, https://doi.org/10.1002/anie.202218016.

[19] D. Xiao, C. Huang, Y. Luo, K. Tang, Q. Ruan, G. Wang, P.K. Chu, Atomic-scale intercalation of graphene layers into $MoSe_2$ nanoflower sheets as a highly efficient catalyst for hydrogen evolution reaction, ACS Appl. Mater. Interfaces 12 (2) (2020) 2460–2468, https://doi.org/10.1021/acsami.9b18302.

[20] K.K. Mandari, N. Son, M. Kang, Synergistic effects of 1T-2H MoS_2 nanoflowers modified with Ag_3PO_4 nanoclusters for highly efficient electrochemical activity, Int. J. Hydrog. Energy 48 (62) (2023) 23842–23855, https://doi.org/10.1016/j.ijhydene.2022.11.309.

[21] D. Xiao, C. Huang, Y. Luo, K. Tang, Q. Ruan, G. Wang, P.K. Chu, Atomic-scale intercalation of graphene layers into $MoSe_2$ nanoflower sheets as a highly efficient catalyst for hydrogen evolution reaction, ACS Appl. Mater. Interfaces 12 (2) (2020) 2460–2468, https://doi.org/10.1021/acsami.9b18302.

[22] Z. Gholamvand, D. McAteer, C. Backes, N. McEvoy, A. Harvey, N.C. Berner, D. Hanlon, C. Bradley, I. Godwin, A. Rovetta, M.E.G. Lyons, G.S. Duesberg, J. N. Coleman, Comparison of liquid exfoliated transition metal dichalcogenides reveals $MoSe_2$ to be the most effective hydrogen evolution catalyst, Nanoscale 8 (10) (2016) 5737–5749, https://doi.org/10.1039/C5NR08553E.

[23] Q. Fu, J. Han, X. Wang, P. Xu, T. Yao, J. Zhong, W. Zhong, S. Liu, T. Gao, Z. Zhang, L. Xu, B. Song, 2D transition metal dichalcogenides: design, modulation, and challenges in electrocatalysis, Adv. Mater. 33 (6) (2021) 1907818, https://doi.org/10.1002/adma.201907818.

[24] S. Deng, F. Yang, Q. Zhang, Y. Zhong, Y. Zeng, S. Lin, X. Wang, X. Lu, C.-Z. Wang, L. Gu, X. Xia, J. Tu, Phase modulation of (1T-2H)-$MoSe_2$/TiC-C shell/core arrays via nitrogen doping for highly efficient hydrogen evolution reaction, Adv. Mater. 30 (34) (2018) 1802223, https://doi.org/10.1002/adma.201802223.

[25] N. Li, J. Wu, Y. Lu, Z. Zhao, H. Zhang, X. Li, Y.-Z. Zheng, X. Tao, Stable multiphasic 1T/2H $MoSe_2$ nanosheets integrated with 1D sulfide semiconductor for drastically enhanced visible-light photocatalytic hydrogen evolution, Appl. Catal. B 238 (2018) 27–37, https://doi.org/10.1016/j.apcatb.2018.07.002.

[26] J. Yi, G. Zhang, X. Cao, X. Zhu, L. Li, X. Wang, X. Zhu, Y. Song, H. Xu, X. Wang, Structurally disordered $MoSe_2$ with rich 1T phase as a universal platform for enhanced photocatalytic hydrogen production, J. Colloid Interface Sci. 668 (2024) 492–501, https://doi.org/10.1016/j.jcis.2024.04.166.

[27] Y. Yu, G.-H. Nam, Q. He, X.-J. Wu, K. Zhang, Z. Yang, J. Chen, Q. Ma, M. Zhao, Z. Liu, F.-R. Ran, X. Wang, H. Li, X. Huang, B. Li, Q. Xiong, Q. Zhang, Z. Liu, L. Gu, Y. Du, W. Huang, H. Zhang, High phase-purity 1T′-MoS_2- and 1T′-$MoSe_2$-layered crystals, Nat. Chem. 10 (6) (2018) 638–643, https://doi.org/10.1038/s41557-018-0035-6.

[28] S. Deng, Y. Zhong, Y. Zeng, Y. Wang, Z. Yao, F. Yang, S. Lin, X. Wang, X. Lu, X. Xia, J. Tu, Directional construction of vertical nitrogen-doped 1T-2H $MoSe_2$/graphene shell/core nanoflake arrays for efficient hydrogen evolution reaction, Adv. Mater. 29 (21) (2017) 1700748, https://doi.org/10.1002/adma.201700748.

[29] Y. Yin, Y. Zhang, T. Gao, T. Yao, X. Zhang, J. Han, X. Wang, Z. Zhang, P. Xu, P. Zhang, X. Cao, B. Song, S. Jin, Synergistic phase and disorder engineering in 1T-$MoSe_2$ nanosheets for enhanced hydrogen-evolution Reaction, Adv. Mater. 29 (28) (2017) 1700311, https://doi.org/10.1002/adma.201700311.

[30] S. Mao, Z. Wen, S. Ci, X. Guo, K. Ostrikov, J. Chen, Perpendicularly oriented $MoSe_2$/graphene nanosheets as advanced electrocatalysts for hydrogen evolution, Small 11 (4) (2015) 414–419, https://doi.org/10.1002/smll.201401598.

[31] A. Ambrosi, Z. Sofer, M. Pumera, 2H → 1T phase transition and hydrogen evolution activity of MoS_2, $MoSe_2$, WS_2 and WSe_2 strongly depends on the MX_2 composition, Chem. Commun. 51 (40) (2015) 8450–8453, https://doi.org/10.1039/C5CC00803D.

[32] W. Li, C. Cheng, J. Zhao, Y. Song, C. Xue, Enhanced azo dye removal through sequential ultrasound-assisted-treatment and photocatalysis using CdZnS, Angew. Chem. Int. Ed. 64 (11) (2025) e202425508, https://doi.org/10.1002/anie.202425508.

[33] G. Zhang, Y. Xu, M. Rauf, J. Zhu, Y. Li, C. He, X. Ren, P. Zhang, H. Mi, Breaking the limitation of elevated coulomb interaction in crystalline carbon nitride for visible and near-infrared light photoactivity, Adv. Sci. 9 (21) (2022) 2201677, https://doi.org/10.1002/advs.202201677.

[34] S. Zuieva, X. Chen, Synthetic approaches to molecule-2D transition metal dichalcogenide heterostructures, Angew. Chem. Int. Ed. 64 (18) (2025) e202424932, https://doi.org/10.1002/anie.202424932.

[35] L. Bai, H. Huang, S. Zhang, L. Hao, Z. Zhang, H. Li, L. Sun, L. Guo, H. Huang, Y. Zhang, Photocatalysis-assisted Co_3O_4/g-C_3N_4 p–n junction all-solid-state supercapacitors: a bridge between energy storage and photocatalysis, Adv. Sci. 7 (22) (2020) 2001939, https://doi.org/10.1002/advs.202001939.

[36] X. Wang, X. Wang, J. Huang, S. Li, A. Meng, Z. Li, Interfacial chemical bond and internal electric field modulated Z-scheme Sv-$ZnIn_2S4$/$MoSe_2$ photocatalyst for efficient hydrogen evolution, Nat. Commun. 12 (1) (2021) 4112, https://doi.org/10.1038/s41467-021-24511-z.

[37] M.Z. Ishaque, Y. Zaman, A. Arif, A.B. Siddique, M. Shahzad, D. Ali, M. Aslam, H. Zaman, M. Faizan, Fabrication of ternary metal oxide (ZnO:NiO:CuO) nanocomposite heterojunctions for enhanced photocatalytic and antibacterial applications, RSC Adv. 13 (44) (2023) 30838–30854, https://doi.org/10.1039/D3RA05170F.

[38] K.K. Mandari, Y. Im, S. Pandey, M. Kang, Transforming solar energy to fuel: innovative Ru@$CuInS_2$/g-C_3N_4 nanocomposites for green hydrogen production, Renew. Energy 256 (2026) 124195, https://doi.org/10.1016/j.renene.2025.124195.